Received: 29 June 2025 | Revised: 10 November 2025 | Accepted: 11 November 2025

DOI: 10.1111/ijac.70119

International Journal of Applied Ceramic Technology

SPECIAL ISSUE ARTICLE

Synthesis and thermal properties of dense Si—Al—C—N-based polymer-derived ceramics

Minoo Boroojerdi[1] | **Daniela Camacho**[1] | **Hergen Breitzke**[2] | **Ingrit Nurak**[3] | **Marc Widenmeyer**[1] | **Wenjie Xie**[1] | **Astrid Pundt**[3] | **Gerd Buntkowsky**[2] | **Ralf Riedel**[1] | **Emanuel Ionescu**[1,4,5]

[1]Institut für Materialwissenschaft, Technische Universität Darmstadt, Darmstadt, Germany

[2]Institut für Physikalische und Theoretische Chemie, Technische Universität Darmstadt, Darmstadt, Germany

[3]Institut für Angewandte Materialien-Werkstoffkunde, Karlsruher Institut für Technologie, Karlsruhe, Germany

[4]Fraunhofer IWKS, Alzenau, Germany

[5]Institut für Chemische Technologien und Analytik, Technische Universität Wien, Wien, Austria

Correspondence
Emanuel Ionescu, Institut für Materialwissenschaft, Technische Universität Darmstadt, Peter-Grünberg-Str. 2, Darmstadt 64287, Germany.
Email: emanuel.ionescu@tu-darmstadt.de

Funding information
German Science Foundation; "MatCom-ComMat: Materials Compounds from Composite Materials for Applications in Extreme Conditions", Grant/Award Number: 413956820

Abstract

In the present study, aluminum-modified preceramic silicon polymers were synthesized via chemical modification of a commercially available organopolysilazane using an aluminum amido complex. The incorporation of aluminum into the polymer structure and its effect on ceramization behavior and processability as well as the thermal and mechanical properties of the obtained Si—Al—C—N ceramic materials were systematically investigated. The microstructure and chemical composition of the dense, predominantly amorphous monolithic Si—Al—C—N were characterized using solid-state nuclear magnetic resonance, scanning electron microscopy, and transmission electron microscopy. Aluminum incorporation led to enhanced densification of Si—C—N, resulting in monoliths with a porosity fraction as low as 2 vol% achieved for the composition with the highest aluminum content. Al incorporation was shown to also result in a significant reduction in thermal conductivity, thus, Si—Al—C—N formulations exhibited values as low as 0.6 W m^{-1} K^{-1}. The hardness and Young's modulus remained nearly unchanged upon aluminum incorporation, with values of ca. 14.5 and 156 GPa, respectively, for the high-aluminum-content sample. To the best of our knowledge, the present study reports for the first time on the thermal and mechanical properties of dense, mainly amorphous Si—Al—C—N ceramics, highlighting the suitability of Si—Al—C—N as excellent material for possible thermal insulation at temperatures beyond 1000°C.

KEYWORDS
polymer precursor, silicon carbonitride, synthesis, thermal conductivity

1 | INTRODUCTION

Thermal barrier coatings (TBCs) are extensively used in high-temperature environments such as gas turbine blades, internal combustion engines (ICEs), and pyrochemical reprocessing systems.[1] Currently, a vast majority of global transportation depends on ICEs, with approximately 95% of transport energy derived from liquid fossil fuels such as gasoline, diesel, and jet fuel.[2] The growing demand for more efficient and environmentally sustainable propulsion systems has intensified research into TBCs for both fossil-fuel-powered and biofuel-driven engines.[3–6] Next-generation TBC materials must exceed the performance of the current benchmark, namely, yttria-stabilized zirconia, which suffers from phase instability and pronounced sintering at temperatures exceeding 1200°C.[7,8]

Standard TBC architectures are typically comprised of a metallic bond coat and a ceramic topcoat and thermally insulate the underlying superalloy substrates, as well as mitigate thermal expansion mismatch by offering sufficient compliance.[9–11] A critical requirement is intrinsically low thermal conductivity, enabling TBCs to provide steep thermal gradients between the combustion atmosphere and the substrate while at the same time ensuring high (thermo)mechanical stability.[7,12]

Synthesis routes for ceramics from polymeric precursors (so-called polymer-derived ceramic [PDC] routes) have been shown in the last decades to offer precise control over chemical composition and nanostructural evolution of the ceramics (PDCs) via tuning of the polymer architecture as well as via tailored thermal treatment conditions during curing and pyrolysis. PDC nanocomposites are typically synthesized using preceramic polymers chemically modified with metal alkoxides, acetylacetonates, acetates, amido complexes, or related compounds.[13,14] Upon pyrolysis at around 1000°C, these precursors convert into amorphous ceramics. Subsequent high-temperature treatments promote phase separation and crystallization, yielding nanocomposites with well-controlled phase compositions and microstructures.[15]

A major advantage of the PDC approach relies on the possibility to engineer single-source precursors with tailored compositions and molecular architecture. Moreover, polymer-based shaping and coating techniques—such as dip coating, spin coating, and injection molding—offer significant flexibility for complex geometries and advanced coating applications.[16–18] Silicon-based PDCs have demonstrated exceptional thermal stability, creep resistance, and thermomechanical performance, making them promising candidates for high-temperature structural applications.[16,19–22] Among silicon-based ceramics, silicon carbonitrides (Si—C—N) are particularly promising for high-temperature structural applications. Si—C—N ceramics are synthesized via pyrolysis of low- or high-molecular-weight polyorganosilazanes or polyorganosilylcarbodiimides.[23,24] A notable characteristic feature of Si—C—N is its ability to retain an amorphous structure up to 1500°C in oxygen-free atmosphere, along with excellent thermal shock resistance, creep resistance, and high-temperature corrosion/oxidation stability.[25,26] SiCN ceramics were shown to possess superior high-temperature oxidation performance upon exposure to temperatures up to 1500°C, which is comparable to that of other non-oxidic ceramics such as Si_3N_4 and SiC. Nonetheless, oxidation and hot corrosion remain serious challenges for silicon-based ceramics, particularly while exposing them to both oxidizing and humid environments.[27–29] Therefore, further chemical modification of Si—C—N ceramics is beneficial to mitigate these disadvantages. For instance, the incorporation of elements such as boron or aluminum into the SiCN matrix has been shown to further reduce oxidation rates and enhance the long-term stability of these ceramics at temperatures above 1400°C, making them highly competitive with and in some cases superior to other state-of-the-art high-temperature ceramic materials.

Si—Al—C—N ceramics, as part of the Si-containing PDC family, exhibit significantly improved resistance to oxidation and hot corrosion as compared to polymer-derived Si—C—N without Al, maintaining their structural stability up to 1200°C.[30–33] Despite these advantageous properties, the broader application of Si-based ceramics is hindered by the substantial evolution of gaseous species during pyrolysis, which can hinder densification as well as microstructure control.[25] Various processing strategies have been explored to address this issue, including hot pressing, hot isostatic pressing of PDC powders, and the shaping of infusible polymers followed by pyrolysis to obtain monolithic PDC components.[34–36] Notably, for the Si—Al—C—N system, Yu et al. introduced an innovative solid–liquid mixing method for precursor preparation, enabling the fabrication of monolithic Si—Al—C—N ceramics with remarkably low porosity of ca. 3.8%.[25]

In this communication, we report for the first time that amorphous dense Si—Al—C—N ceramics possess exceptionally low intrinsic thermal conductivity (as low as 0.6 W m^{-1} K^{-1}). Dense, crack-free, and amorphous Si—Al—C—N monoliths were prepared via uniaxial pressing of polymeric single-source precursors synthesized from a commercially available poly(organo)silazane (Durazane 1800) chemically modified with an aluminum dimethylamido complex followed by pressureless pyrolysis. The

effect of aluminum incorporation into Si—C—N on its densification behavior and thermal properties was systematically investigated.

2 | EXPERIMENTAL PROCEDURE

2.1 | Materials synthesis and processing

Single-source precursors for Si—Al—C—N ceramics were synthesized using the Schlenk technique under an argon atmosphere. Commercially available polysilazane Durazane 1800 (Merck) and tris(dimethylamido)aluminum $Al[N(CH_3)_2]_3$ (TDMAA, Sigma–Aldrich) were each dissolved separately in anhydrous toluene (Sigma–Aldrich). The TDMAA solution was added dropwise to the Durazane 1800 solution at room temperature under continuous stirring. Two mass ratios of Durazane 1800 to TDMAA were employed, that is, 10.8:1 and 5.4:2. The mixtures were stirred for 24 h at ambient temperature, after which the solvent was removed under vacuum. The resulting viscous precursors—yellow to orange in color—are referred to as Al1- and Al2-Durazane 1800, for the two employed Durazane 1800:TDMAA ratios of 10.8:1 and 5.4:2, respectively. The single-source precursors were crosslinked at 250°C for 3 h, followed by pyrolysis at 1000°C for 4 h under argon, using a heating rate of 300°C h^{-1}. To further examine thermal stability and microstructural evolution, the pyrolyzed powders were annealed under nitrogen at 1200°C, 1400°C, and 1500°C for 4 h each.

Green bodies were fabricated using a mixture of aluminum-modified polymeric precursor and crosslinked preceramic powder, following a procedure similar to that reported by Yu et al.[25] In their study, the lowest porosity (~3.82 vol%) was achieved in a bulk ceramic sample prepared from a solid–liquid mixture with a volume ratio of 30:1. In the present work, a solid–liquid volume ratio of 3:1 was selected to improve densification. The fabrication process included grinding and sieving of the crosslinked Durazane 1800 and Al1- and Al2-Durazane 1800 powders using a 0.032 mm mesh. The resulting fine powder was then mixed with the corresponding liquid polymer and liquid Al1- and Al2-Durazane 1800 precursor and transferred into a cylindrical mold (10 mm diameter). Uniaxial pressing was applied at room temperature (70 MPa for 10 min). Subsequently, the green bodies (Figure 1D) were cold isostatically pressed at 250 MPa for 5 min and pyrolyzed at 1000°C for 4 h under 1 bar argon atmosphere to deliver dense and crack-free Si—Al—C—N-based ceramic monoliths (Figure 1E).

2.2 | Material characterization

The as-synthesized Al1- and Al2-Durazane 1800 precursors were characterized by Fourier-transform infrared spectroscopy (FTIR; Varian 670-IR, Agilent) in attenuated total reflectance mode, both before and after crosslinking. To analyze the polymer-to-ceramic transformation, thermogravimetric analysis (TGA; STA 449C Jupiter, Netzsch) was carried out in combination with quadrupole mass spectrometry (QMS 403C Aëolos, Netzsch). The measurements were performed under flowing argon at a heating rate of 5°C min^{-1} from room temperature to 1000°C. The resulting PDC powders, SiAlCN1 and SiAlCN2, were further analyzed using various characterization techniques. Solid-state nuclear magnetic resonance (NMR) spectra were recorded on a Bruker Avance II+ 400 MHz spectrometer at 9.4 T, which corresponds to a frequency of 400.13 MHz for ^{1}H. The spectrometer was equipped with a Bruker 4 mm H/X MAS probe. ^{29}Si spectra were recorded utilizing the Bruker zg0ig pulse sequence with 30° flip angle, relaxation delay of 20 s, spinning speed of 10 kHz, and were referenced with respect to Kaolin at −92.5 ppm as external standard. TPPM15 ^{1}H decoupling was applied during data acquisition. A 250 Hz exponential line broadening was applied before Fourier transformation. ^{27}Al spectra were recorded utilizing the Bruker zg0ig pulse sequence with 20° flip angle, relaxation delay of 1 s, spinning speed of 10 kHz, and were referenced with respect to a solution of $AlCl_3$ in D_2O at 0 ppm as external standard. No ^{1}H decoupling was applied during data acquisition. A 25 Hz exponential line broadening was applied before Fourier transformation. Phase analysis was conducted by X-ray diffraction (XRD) in transmission mode using a STOE STADI MP diffractometer (Mo $K\alpha_1$ radiation with Ge (111) monochromator, STOE). Micro-Raman spectroscopy was performed using a LabRAM HR8000 spectrometer (Horiba Jobin Yvon) with a 514.5 nm excitation wavelength. Sample preparation for scanning electron microscopy (SEM) and transmission electron microscopy (TEM) followed standard ceramographic procedures, including cutting, grinding, and polishing (SiC abrasive papers of grit size P2400, FEPA standard). TEM was conducted using a Philips CM200 (Philips) operated at an accelerating voltage of 200 kV and equipped with an energy-dispersive X-ray spectroscopy detector (SDD-X-Max 80, Oxford). Selected area electron diffraction was employed to obtain structural information on the constituent phases within the bulk ceramic sample. Surface morphology was examined by high-resolution scanning electron microscopy (HR-SEM; JSM-7600F, JEOL Ltd.), and backscattered electron (BSE) images were acquired at an accelerating voltage of

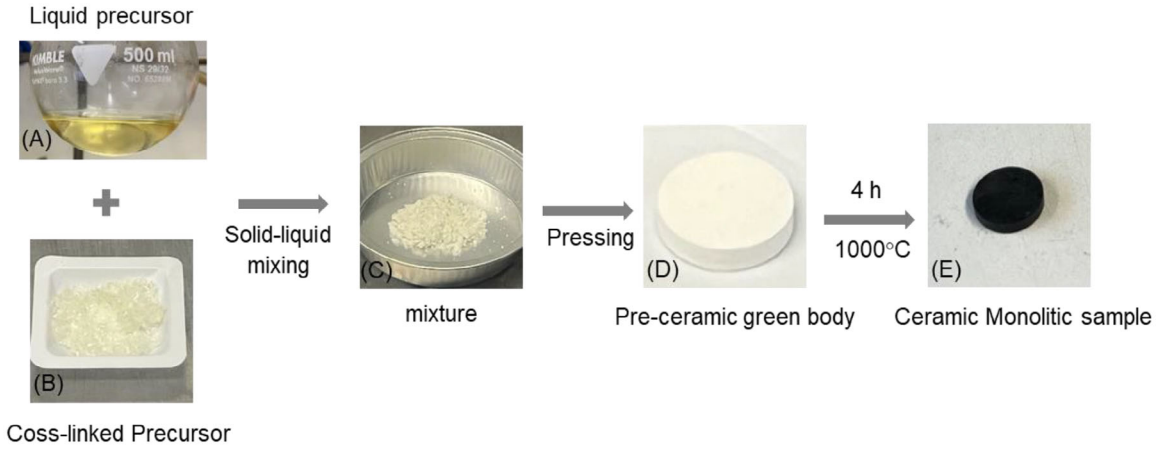

FIGURE 1 Schematic fabrication of the Si—Al—C—N-based ceramic monolithic samples from polymer-derived precursors. (A) Liquid polymer precursor, (B) cross-linked precursor powder, (C) solid–liquid mixture, (D) pre-ceramic green body obtained by pressing, and (E) final ceramic monolith after pyrolysis at 1000°C for 4 h.

15 kV. Elemental analysis of the ceramics was conducted to determine the carbon, nitrogen, and oxygen contents. Carbon concentration was measured using a LECO C-200 analyzer (LECO Corporation) via hot gas extraction. Nitrogen and oxygen contents were determined using an ELEMENTRAC ONH-p2 analyzer (Eltra Elemental Analyzers, Verder Scientific GmbH). Quantitative analysis of aluminum content was carried out via inductively coupled plasma optical emission spectroscopy (ICP-OES) at Mikroanalytisches Labor Pascher. The bulk density and open porosity of the samples were measured using the Archimedes method. Thermal diffusivity of the bulk samples was evaluated by laser flash analysis (LFA; 457 MicroFlash, Netzsch-Gerätebau GmbH) from room temperature up to 900°C under an argon atmosphere, using a heating rate of 10°C min^{-1}. The specific heat capacity (C_p) was determined by differential scanning calorimetry (DSC) using a DSC 404 F1 Pegasus (Netzsch-Gerätebau GmbH) over the same temperature range and heating conditions. For nanoindentation, a G200 Nano indenter (KLA-Tencor) with a maximum load of 3000–3500 mN (average penetration depth of 3000 nm) equipped with a Berkovich indenter tip was used to obtain average reduced Young's moduli. The Young's modulus was calculated from the reduced moduli (a Poisson's ratio of 0.18 was assumed).[37]

3 | RESULT AND DISCUSSION

3.1 | Synthesis of single-source precursors

As described in the experimental section, the Al1- and Al2-Durazane 1800 precursors were synthesized by reacting Durazane 1800 with $Al[N(CH_3)_2]_3$ in two different concentrations. The FTIR spectra of the single-source precursors are shown in Figure 2A. The main absorption bands include N–H (3376 cm^{-1}), C–H (2953 cm^{-1}), Si–H (2119 cm^{-1}), C═C (1592 cm^{-1}), $Si–CH_3$ (1252 cm^{-1}), Si–N–H (1165 cm^{-1}), Si–N–Si (889 cm^{-1}), and Si–C (751 cm^{-1}), which are also present in pure Durazane 1800.[15,38,39] The functional Si–H and N–H groups in the poly(organo)silazane react with tris(dimethylamido)aluminum to form Si–N–Al bonds.[15,40,41] The FTIR spectrum of the aluminum-modified Durazane 1800 shows a decrease in the intensity of the N–H and Si–H bands, although these signals do not disappear entirely, indicating that substitution with TDMAA does not fully consume the N–H and Si–H groups at room temperature.[15,38] The liquid Al1- and Al2-Durazane 1800 precursors were crosslinked at 250°C to investigate the intermediate stage of the initial ceramization process. The FTIR spectra of the crosslinked precursors are presented in Figure 2B. A noticeable decrease in the intensities of the Si–H and N–H stretching bands, as well as the C═C vibration bands, was observed after thermal treatment compared to unmodified Durazane 1800. This reduction was more pronounced in the crosslinked Al2-Durazane 1800 sample, suggesting that a higher TDMAA content promotes more extensive reactions between Si–H/N–H groups and the aluminum precursor, resulting in a greater degree of crosslinking. Additionally, hydrosilylation reactions, in which the reactive functional groups are consumed, take place, leading to a solid-state crosslinking within the preceramic network.[38]

In the FTIR spectra of the Al-modified polysilazanes (Al1- and Al2-Durazane 1800), a broad and shallow absorption band appears in the ~920–940 cm^{-1} region, which is absent in the unmodified precursor. This band is attributed to Al–N stretching vibrations, which often overlap with Si–N modes in polymer-derived Si–Al–C–N ceramics.

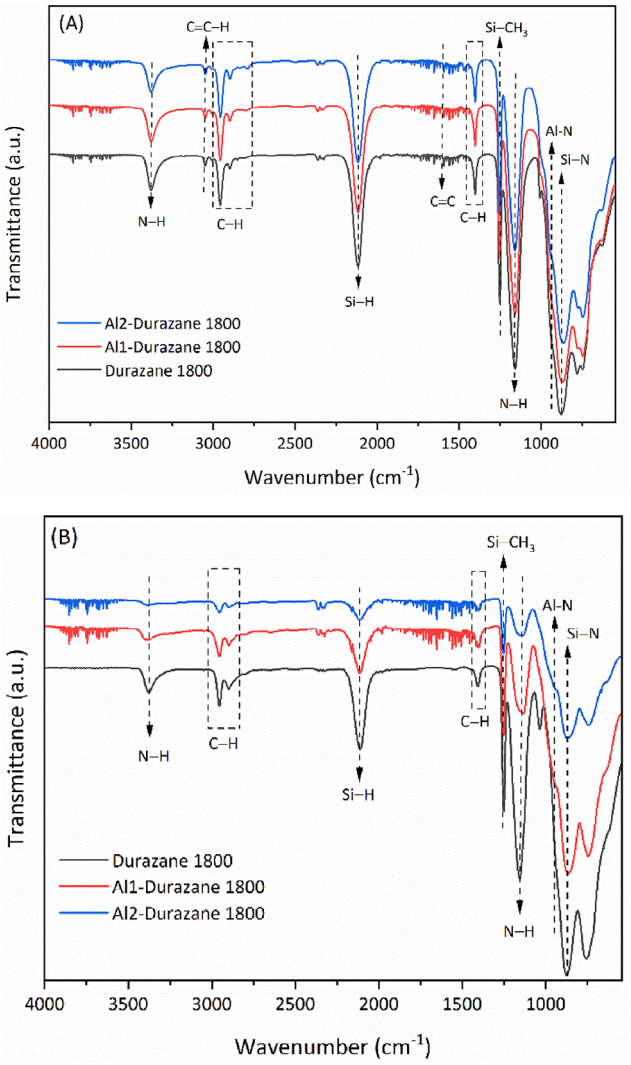

FIGURE 2 Fourier-transform infrared spectroscopy (FTIR) spectra of Durazane 1800 and Al1- and Al2-Durazane 1800 at: (A) room temperature (RT) (i.e., pre-crosslinking), and (B) after thermal treatment at 250°C (i.e., post-crosslinking).

Berger et al. reported a broad Al–N-related absorption centered around 806 cm^{-1}, extending toward higher wavenumbers up to ~1000 cm^{-1}, and emphasized that in amorphous ceramic systems, Al–N and Si–N vibrations cannot be distinctly resolved due to significant spectral overlap and band broadening.[42] Similarly, Salameh et al. highlighted the general complexity of the 500–1200 cm^{-1} region, noting that Si–N and Al–N contributions coexist and are difficult to distinguish individually in amorphous Si—Al—C—N networks.[43] In the synthesized Al-modified precursors, the Al–N-related band in the 920–940 cm^{-1} region is barely distinguishable at room temperature but becomes more pronounced and clearly visible after thermal crosslinking at 250°C, indicating the progressive formation of Al–N bonds during the early stages of polymer-to-ceramic conversion. Additionally, a

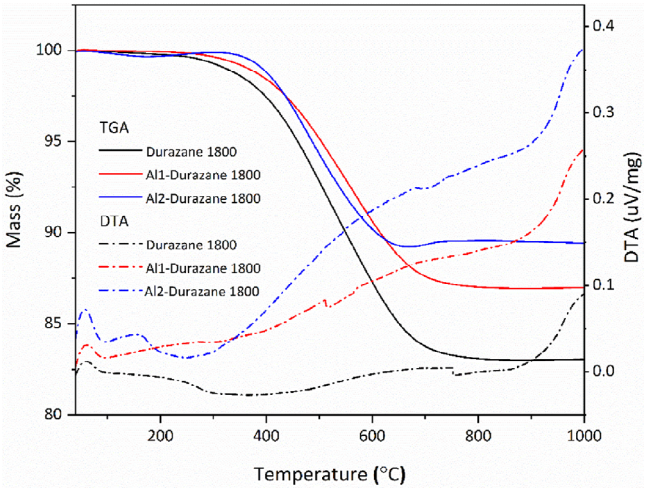

FIGURE 3 Thermogravimetric analysis (TGA) and differential thermal analysis (DTA; upward peaks correspond to exothermic processes) of Durazane 1800 and Al1- and Al2-Durazane 1800 samples at a heating rate of 10°C min^{-1} in flowing argon.

decrease in the intensity of the C–H vibration bands further supports the enhanced crosslinking effect induced by the incorporation of a higher concentration of the aluminum metal amide complex into Durazane 1800 polymer network.

3.2 | Polymer-to-ceramic transformation

The ceramization behavior of Al1- and Al2-Durazane 1800 was investigated and compared to that of the unmodified Durazane 1800 using TGA coupled with evolved gas analysis. To minimize the effects of hydrolysis, TGA measurements were carried out on crosslinked powders obtained after heat treatment at 250°C. As shown in Figure 3, the ceramization process is considered complete at approximately 800°C, as indicated by the stabilization of the mass loss in the TGA curves, marking the end of major decomposition and the transition to a stable ceramic network. The ceramization yield of Durazane 1800 (at 1000°C) is approximately 83%, and the incorporation of the aluminum amide complex leads to an increased ceramic yield. Al2-Durazane 1800, containing a higher amount of TDMAA, exhibited the highest ceramic yield of approximately 90%. The differential thermal analysis curve reveals an exothermic peak beginning around 75°C in all three samples. This behavior is primarily attributed to hydrosilylation reactions occurring at low temperatures (starting around 100°C–120°C) between Si–H functional groups in Durazane 1800 and vinyl groups, leading to the formation of Si–C linkages.[15,22,41]

The analyzed volatile species released during the structural transformation are shown in Figure 4. The ceramization of Durazane 1800 (Figure 4A) and Al1-Durazane 1800 (Figure 4B) followed similar decomposition pathways. In the temperature range of approximately 250°C–680°C, a significant release of CH_4 (m/z = 12–16) was observed. Additionally, volatile species with m/z = 24–30 were detected between ~180°C and 680°C and attributed to ethane and ethene gas evolution. Previous studies on the ceramization of Durazane 1800 have linked methane release to rearrangement reactions involving ≡Si–CH_3 and ═N–H groups,[15,41] while ethane evolution is associated with reactions between Si-vinyl-substituted polysilazanes and ═N–H groups. Furthermore, transamination reactions between ≡Si–N═ and ═Al–N═ groups in the Al-containing samples may contribute to the evolution of amine fragments. The thermal decomposition of the aluminum amido complex, $Al(NMe_2)_3$, is also a likely source of amine-containing volatiles in both Al1- and Al2-Durazane 1800. Only minor differences were observed in the polymer-to-ceramic transformation of Al2-Durazane 1800, as shown in Figure 4C. Notably, hydrogen (H_2^+; m/z = 2) was released over the entire temperature range. This release is attributed to dehydrocoupling reactions between ≡Si–H and ═N–H groups, as well as the decomposition of hydrocarbon substituents. Additionally, the evolution of amine fragments (m/z = 41, 42) was more pronounced in Al2-Durazane 1800, suggesting that its higher degree of crosslinking increases susceptibility to transamination reactions.[15,41] Finally, the Al2-Durazane 1800 sample exhibits a pronounced m/z = 44 signal, corresponding to CO_2 evolution, at elevated temperature range of ca. 550°C–800°C (Figure 4C). The observed CO_2 release reflects the progressive combustion of excess carbon in the high-carbon-content SiAlCN2 sample, consistent with its significantly elevated C_{free} volume fraction of 28.8 vol% (Table 1). In all samples, the evolution of ammonia (m/z = 17) and water (m/z = 18) were detected, confirming the successive polycondensation and transamination reactions with increasing temperature and the final formation of Si—C—N and Si—Al—C—N ceramic networks.[40]

The Raman spectra of the ceramic powder samples annealed at 1200°C, 1400°C, and 1500°C are shown in Figure 5. The absorption bands at ~1360 cm^{-1} (D band) and ~1580 cm^{-1} (G band) analyzed in the 1200°C–1400°C range indicate the presence of disordered carbon (D band) and the in-plane bond stretching of sp^2-hybridized carbon (G band).[41,43,45] Additionally, overtone bands at ~2670 cm^{-1} (2D mode) and ~2900 cm^{-1} (D + D′ mode) were present in all samples up to 1400°C. The integrated intensity of the D band was significantly higher than that of the G band, reflecting the highly disordered nature of the segregated carbon phase.[41,43] After annealing at

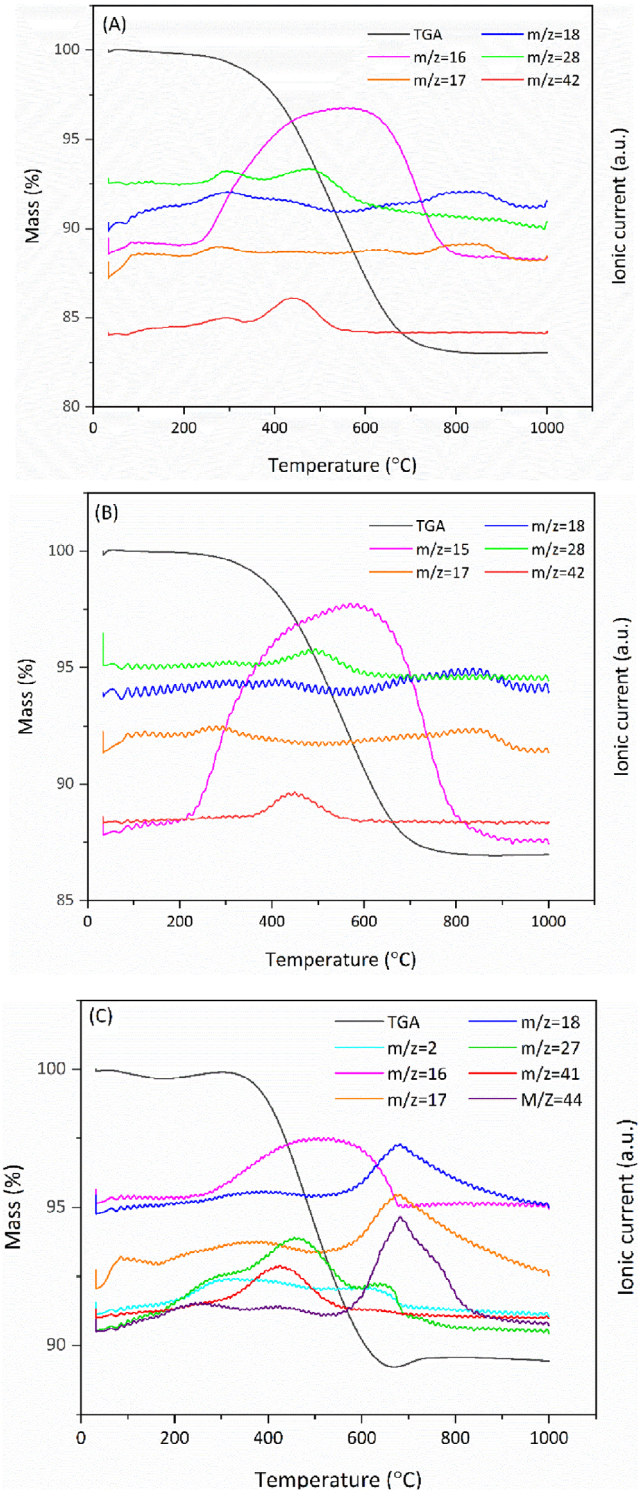

FIGURE 4 Thermogravimetric analysis curve (TGA) and quasi-multiple ion detection (QMID) ion current curves for crosslinked Durazane 1800 (A), Al1-Durazane 1800 (B), and Al2-Durazane 1800 (C). For the sake of clarity, the most intense and representative m/z fragment was selected for plotting each gas species detected.

TABLE 1 Elemental contents of carbon, nitrogen, oxygen, and aluminum[a], as well as volume fractions of the different phases (calculated based on the empirical formulas and considering the densities of the constituting phases: SiC [3.1 g cm^{-3}], SiO_2 [2.2 g cm^{-3}], Si_3N_4 [3.0 g cm^{-3}], and free carbon [1.5 g cm^{-3}][44]) for the SiCN, SiAlCN1, and SiAlCN2 samples at different temperatures.

Sample	Annealing temperature (°C)	C (wt.%)	N (wt.%)	O (wt.%)	Elemental composition	Volume fraction (%)			
						SiO_2	Si_3N_4	SiC	C_{free}
SiCN	1000	18.1 ± 0.3	23.2 ± 0.6	4.2 ± 0.3	$SiO_{0.13}C_{0.77}N_{0.85}$ + 0.47C_{free}	9.20 ± 1.03	51.40 ± 3.63	19.90 ± 1.88	19.60 ± 1.85
	1200	17. ± 0.3	25.5 ± 4.0	0.58 ± 0.07	$SiO_{0.017}C_{0.71}N_{0.90}$ + 0.38C_{free}	1.30 ± 0.15	58.82 ± 4.16	22.89 ± 2.16	17.00 ± 1.60
	1400	16.4 ± 0.7	26.3 ± 2.0	0.470 ± 0.002	$SiO_{0.014}C_{0.67}N_{0.92}$ + 0.36C_{free}	1.08 ± 0.12	60.60 ± 4.29	22.08 ± 2.08	16.24 ± 1.53
SiAlCN1	1000	18.1 ± 0.4	20.8 ± 0.1	1.06 ± 0.02	$SiO_{0.032}Al_{0.042}C_{0.73}N_{0.72}$ + 0.28C_{free}	2.60 ± 0.17	49.96 ± 3.37	34.11 ± 2.94	13.31 ± 0.95
	1200	16.6 ± 0.5	28.1 ± 0.7	1.26 ± 0.09	$SiO_{0.042}Al_{0.047}C_{0.76}N_{1.08}$ + 0.59C_{free}	2.85 ± 0.28	62.76 ± 6.54	10.90 ± 0.94	23.50 ± 2.12
	1400	16.7 ± 0.5	25.5 ± 1.6	0.47 ± 0.04	$SiO_{0.014}Al_{0.044}C_{0.71}N_{0.93}$ + 0.41C_{free}	1.05 ± 0.15	59.74 ± 4.75	21.00 ± 2.11	18.22 ± 1.08
SiAlCN2	1000	17.8 ± 0.1	27.2 ± 1.0	3.8 ± 0.1	$SiO_{0.14}Al_{0.96}C_{0.88}N_{1.16}$ + 0.82C_{free}	8.32 ± 0.49	59.42 ± 3.53	3.4 ± 0.2	28.80 ± 1.71
	1200	15.4 ± 0.1	22.2 ± 0.9	2.40 ± 0.02	$SiO_{0.075}Al_{0.081}C_{0.64}N_{0.79}$ + 0.27C_{free}	5.95 ± 0.36	53.66 ± 3.25	27.82 ± 1.69	12.57 ± 0.76
	1400	17.7 ± 0.1	28.3 ± 2.5	1.8 ± 0.2	$SiO_{0.067}Al_{0.094}C_{0.86}N_{1.18}$ + 0.77C_{free}	4.17 ± 0.53	62.89 ± 7.99	4.81 ± 0.61	28.13 ± 3.57

[a]Across the entire temperature range of 1000°C–1400°C, a constant aluminum content of 2.38 ± 0.01 wt% and 4.37 ± 0.01 wt% was assumed for SiAlCN1 and SiAlCN2, respectively, based on ICP-OES measurements performed with the sample obtained at 1000°C.

FIGURE 5 Raman spectra of SiCN, SiAlCN1, and SiAlCN2 samples annealed at 1200°C (A), 1400°C (B), and 1500°C (C).

1500°C, the intensities of the D and G bands were markedly reduced, and the 2D and D + D′ overtone bands nearly disappeared after 4 h of annealing, indicating a substantial reduction in segregated carbon content. Instead, a characteristic SiC (~790 cm^{-1}) band appeared.[15] Notably,

the SiAlCN2 sample still exhibits features of segregated carbon, suggesting that the reaction between Si_3N_4 and carbon is suppressed by the higher aluminum content, in contrast to the behavior of samples SiAlCN1 and SiCN.

Elemental analysis was performed on SiCN, SiAlCN1, and SiAlCN2 ceramic powder samples. Table 1 presents the chemical composition and the derived empirical formulas of the ceramics obtained at 1000°C, 1200°C, and 1400°C. The aluminum content was measured only for the sample annealed at 1000°C and assumed constant across the temperature series (1000°C–1400°C). For each composition silicon was calculated then as balance to 100 wt%, assuming no other elements were present. No significant changes in the concentrations of carbon, nitrogen, or oxygen were found with increasing temperature up to 1400°C, suggesting that the carbothermal reaction is not dominant at these temperatures and clearly indicating the thermal stability of the Si—Al—C—N ceramic system.

The XRD patterns of SiCN, SiAlCN1, and SiAlCN2 materials annealed at temperatures ranging from 1200°C to 1500°C, with an isothermal hold of 4 h at each temperature, are shown in Figure 6. At 1200°C, the SiCN and SiAlCN2 samples remain X-ray amorphous. However, the XRD pattern of the SiAlCN1 sample exhibits broad reflections corresponding to nanosized β-SiC crystallites.[43,45] At 1400°C, SiCN retains its amorphous structure, while the diffraction peaks of β-SiC become more intense in SiAlCN1 and begin to emerge in the SiAlCN2 sample. Upon further increasing the temperature to 1500°C, the intensity of the β-SiC reflections decreases noticeably in both SiCN and SiAlCN1. Instead, new diffraction peaks corresponding to AlN and β-Si_3N_4 appear. Salameh et al. reported that nanoscale SiC crystallites tend to form preferentially at the expense of Si_3N_4.[43] The attenuation of SiC crystallinity at higher aluminum concentrations may be attributed to the competitive formation of AlN and β-Si_3N_4.

The findings from the XRD measurements were substantiated by TEM results (Figure 7). Thus, SiCN and SiAlCN1 (Figure 7A,B) prepared via pyrolysis at 1000°C were found to be mainly amorphous in nature. While SiAlCN2 prepared at 1000°C (Figure 7C,D) exhibited minor amounts of nanocrystalline β-SiC, thus indicating an effect of Al presence on the partitioning and crystallization of silicon carbide. Sample SiAlCN2 exposed to 1400°C also showed the presence of β-SiC (Figure 7E).

3.3 | Microstructure and thermal properties of dense monolithic Si—Al—C—N-based ceramic samples

To prepare dense and crack-free monolithic ceramic samples, preceramic green bodies were fabricated as described earlier in Section 2.2. Using a solid-to-liquid volume ratio of 3:1, crack-free ceramic monoliths were successfully obtained. The density and open porosity of the monolithic samples were evaluated using the Archimedes method, and the results are summarized in Table 2. The effect of Al incorporation into Si—C—N on its densification during the pyrolysis is evident. Thus, the Al-free sample exhibits an open porosity fraction of ca. 22.3 vol%, whereas the

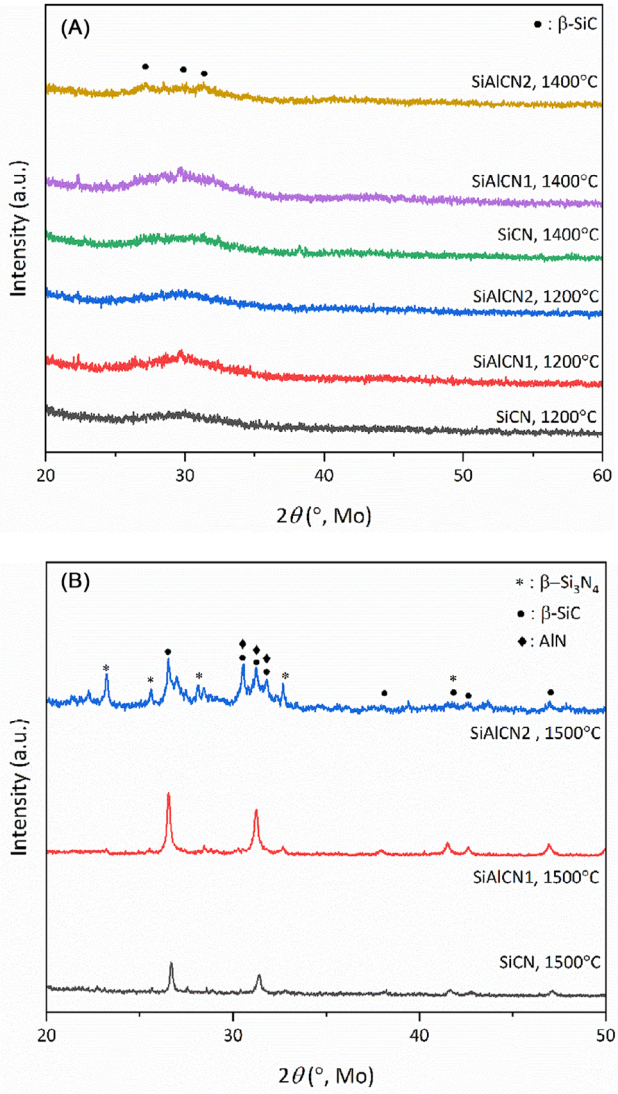

FIGURE 6 X-ray diffraction (XRD) patterns of SiCN, SiAlCN1, and SiAlCN2 annealed at 1200°C and 1400°C (A) and 1500°C (B).

TABLE 2 Bulk density, skeletal density, and porosity of monolithic SiCN, SiAlCN1, and SiAlCN2 at room temperature.

Sample	Bulk density (g cm^{-3})	Skeletal density (g cm^{-3})	Open porosity (vol%)
SiCN	1.763 ± 0.02	2.268 ± 0.05	22.26 ± 1.7
SiAlCN1	2.043 ± 0.06	2.139 ± 0.03	4.51 ± 0.49
SiAlCN2	2.123 ± 0.01	2.174 ± 0.01	2.32 ± 0.62

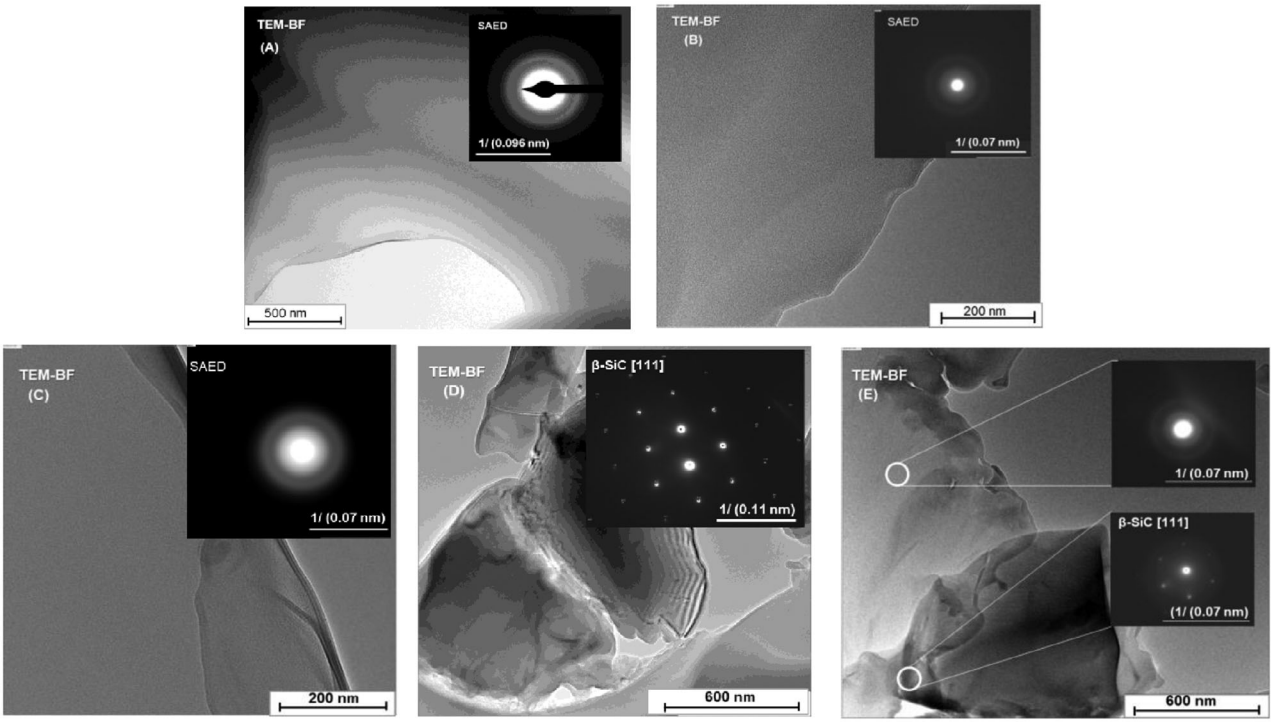

FIGURE 7 Bright field transmission electron microscopy (TEM) micrographs and selected area electron diffraction (SAED) patterns for SiCN (A) and SiAlCN1 (B) prepared upon pyrolysis at 1000°C as well as for SiAlCN2 prepared via pyrolysis at 1000°C (C and D) and 1400°C (E).

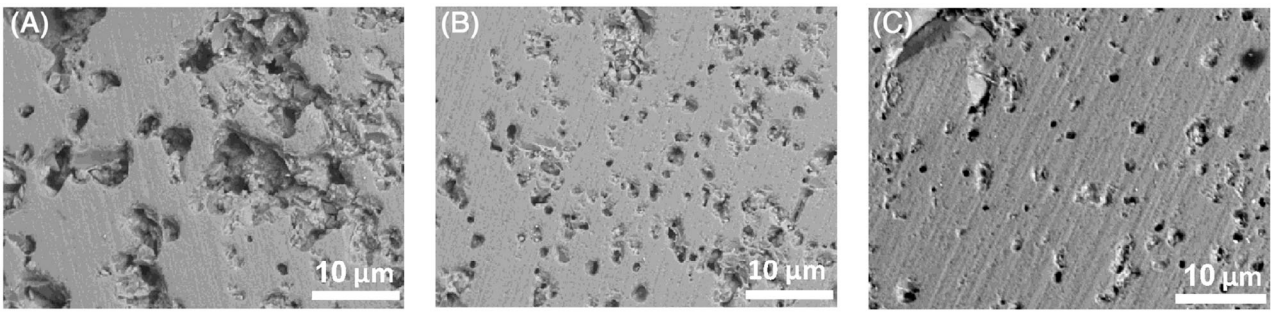

FIGURE 8 Scanning electron microscopy (SEM)–backscattered electron (BSE) image of monolithic SiCN (A), SiAlCN1 (B), and SiAlCN2 (C).

Al-containing samples had porosities of ca. 4.5 and ca. 2.3 vol% for SiAlCN1 and SiAlCN2, respectively. This result is considered to correlate with an increased crosslinking degree of the Al-containing single-source precursor, which consequently results in a lower weight loss during pyrolysis and thus leads to lower porosities, as shown in other metal-modified Si—O—C and Si—C—N systems.[22]

The microstructure of the prepared bulk samples was examined using HR-SEM. Figure 8 shows SEM–BSE images of SiCN, SiAlCN1, and SiAlCN2 after surface polishing. SEM analysis reveals a heterogeneous microstructure consisting of two distinct regions: a continuous matrix phase, likely originating from the preceramic polymer powder, and a dispersed phase composed of partially sintered or embedded domains derived from the solid–liquid mixture. This biphasic morphology results from the precursor architecture, where the initial 3:1 volumetric ratio of crosslinked powder to polymer led to the formation of an inhomogeneous green body during ceramization. The polymer-rich regions underwent thermal decomposition, leading to densification and partial gas release, while the powder-rich regions retained a more fragmented structure. The resulting microstructure reflects the legacy of the processing route, with ceramic conversion occurring unevenly across the matrix and dispersed phases. Aluminum modification significantly influences the resulting microstructure. SiCN (A) displays a more heterogeneous morphology, comprising a matrix and dispersed domains

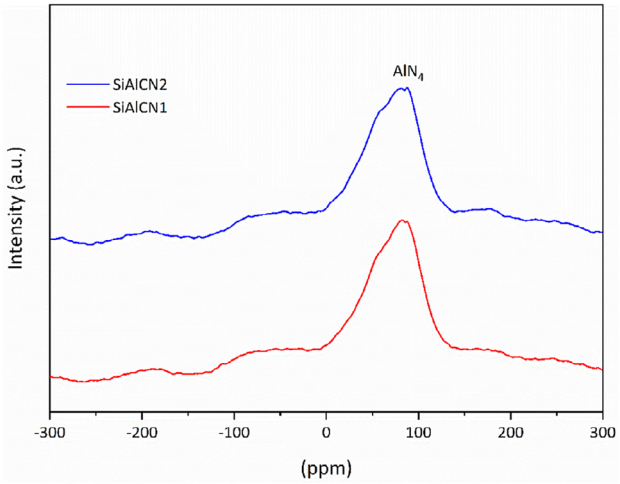

FIGURE 9 ^{27}Al MAS nuclear magnetic resonance (NMR) spectra of SiCN (A), SiAlCN1 (B), and SiAlCN2 (C) ceramic bulk samples.

and large pores concentrated near their interfaces. In contrast, the Al-modified samples (B) and (C) exhibit a more uniform microstructure, with reduced porosity and less distinct phase boundaries. This finding suggests that aluminum promotes network formation, leading to more homogeneous ceramization. Moreover, an increase in the aluminum content resulted in a measurable reduction in porosity, with the SiAlCN2 sample showing ca. 2.3 vol% porosity compared to ca. 4.5 vol% in SiAlCN1, as discussed above (Table 2).

The ^{27}Al MAS NMR spectra of SiAlCN1 and SiAlCN2 (Figure 9) exhibit a chemical shift at approximately ~80 ppm, indicating the presence of tetrahedrally coordinated aluminum (AlN_4). This observation is consistent with previous studies on polymer-derived Si—Al—C—N ceramics, where Al–N coordination environments are stabilized after pyrolysis at 1000°C. Berger et al. reported AlN_4 units giving rise to a resonance near 100 ppm in Al-modified polysilazanes and emphasized that distinguishing AlN from other coordination states becomes increasingly difficult in the amorphous ceramic state due to local disorder and spectral broadening.[42] Furthermore, the chemical shift of the central transition will be influenced by second-order quadrupolar interaction, strongly dependent on local distortions. The apparent chemical shift given in the 1D spectra may differ. Similarly, Salameh et al. assigned the main resonance at ~110 ppm to tetrahedral AlN_4 coordination in aluminum-modified Si—Al—C—N pyrolyzed at 1000°C.[43] Song et al. also observed Al–N coordination in the tetrahedral range (~66 ppm) following pyrolysis at 1000°C in aluminum-modified polysilacarbosilane precursors.[45] Although their shift was slightly lower, they attributed it to the influence of surrounding Si–C–N network bonding and confirmed that tetrahedral AlN_4 remains the dominant coordination at 1000°C. This resonance confirms that aluminum is incorporated as a network-forming species in the amorphous Si–Al–C–N matrix at 1000°C. This interpretation is further supported by FTIR analysis, where a shallow band in the 920–940 cm^{-1} region of the Al-containing samples (Figure 2) correlates with the formation of Al–N linkages during crosslinking.

The ^{29}Si MAS NMR spectra of SiCN, SiAlCN1, and SiAlCN2 (Figure 10) show broad resonances characteristic of amorphous PDCs. Three major peaks are observed: a strong signal around −45 to −48 ppm, corresponding to SiN_4 units; a peak near −25 ppm, attributed to $SiCN_3$ coordination; and another around −17 to −20 ppm, assigned to SiC_4 tetrahedra. These chemical shift assignments are consistent with prior studies on polymer-derived Si—C—N materials, where the local bonding environment of silicon strongly influences the observed resonances.[40,46] A comparison of the spectra of SiAlCN1 and SiAlCN2 reveals distinct structural differences as a function of aluminum content. In SiAlCN1, which contains less aluminum, the peaks corresponding to SiN_4 (−45 to −48 ppm) and $SiCN_3$ (−25 ppm) are both prominent and comparable in intensity, while the SiC_4 peak (−17 to −20 ppm) is significantly lower. This pattern indicates a relatively balanced silicon coordination environment, with mixed N and C bonding. In contrast, SiAlCN2, with a higher aluminum content, displays a dominant SiN_4 signal and a pronounced increase in SiC_4 intensity, exceeding that of $SiCN_3$. This shift is attributed to aluminum's role in network restructuring: Al preferentially forms Al–N–Si bridges, effectively reducing the availability of nitrogen for Si–N–C linkages and thus suppressing $SiCN_3$ formation. The resulting network shows enhanced nitrogen-rich (SiN_4) and carbon-rich (SiC_4) units, at the expense of mixed coordination. A similar rearrangement has been reported in hafnium-modified Si–Hf–C–N–O systems, where increasing metal content favored fully nitrided Si sites.[40] Furthermore, Sen and Widgeon observed that changes in the distribution of SiC_xN_y tetrahedra directly reflect shifts in crosslinking efficiency and network dimensionality, with increased homogeneity in metal-rich systems.[46]

The prepared ceramic monoliths were studied concerning their thermal transport properties. To describe the temperature-dependent thermal conductivity of the studied samples, Equation (1) was used:

$$\lambda(T) = \alpha(T) \cdot C_p(T) \cdot \rho(T) \quad (1)$$

where $\lambda(T)$ represents the thermal conductivity, $\alpha(T)$ denotes the thermal diffusivity, $C_p(T)$ signifies the specific heat capacity, and $\rho(T)$ corresponds to the

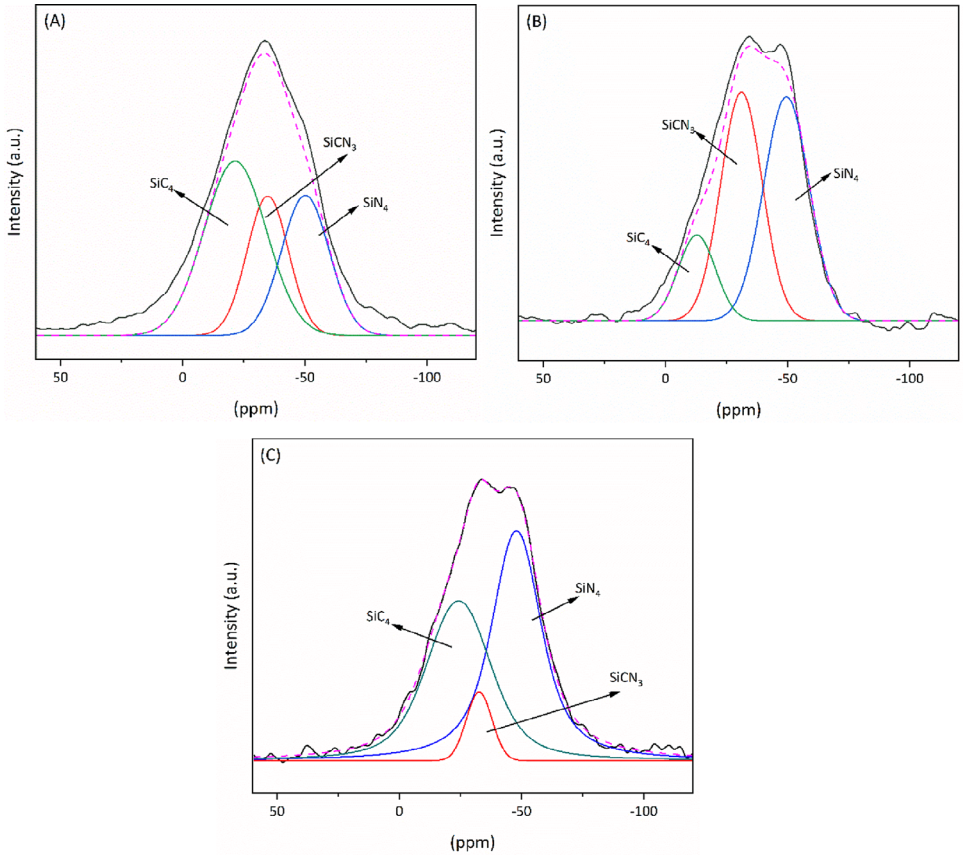

FIGURE 10 ^{29}Si MAS nuclear magnetic resonance (NMR) spectra of SiCN (A), SiAlCN1 (B), and SiAlCN2 (C) ceramic bulk samples.

temperature-dependent density. The temperature-dependent specific heat capacity and thermal diffusivity were determined using DSC and LFA, respectively, while the density was assumed to be temperature independent as simplification.

The evolution of specific heat capacity with increasing temperature for the ceramic monolithic SiAlCN1 and SiAlCN2 samples is shown in Figure 11B. Due to the high porosity (~23 vol%) of the unmodified Si—C—N sample, reliable measurement of its specific heat capacity was not possible, and consequently, its thermal conductivity could not be determined. Thus, for comparison purposes, the specific heat capacity and thermal conductivity values reported in the literature for dense Si—C—N ceramics were used.[44] The specific heat capacity of both Al-containing samples increases steadily with temperature and reaches a plateau at higher temperatures around ca. 1.45 J g^{-1} K^{-1}. These values are clearly higher than those reported for β-SiC[40] and β-Si_3N_4.[47] At 900°C, the specific heat capacity of SiAlCN2 is comparable to the reported value for Si—C—N ceramic formulations.[44] In contrast, the temperature-dependent specific heat capacity of SiAlCN1 is significantly higher than that of the SiAlCN2. This can be attributed to its greater structural heterogeneity and a higher fraction of sp^3-hybridized environments (Figure 10), which introduce a broader distribution of low-energy vibrational modes. These disorder bonding motifs are known to enhance the configurational entropy and thus, the heat storage ability.[39] In comparison, the more ordered and rigid bonding landscape dominated by SiN_4 units in SiAlCN2 supports fewer low-frequency phonons, leading to a lower measured specific heat capacity. Figures 11A,C summarize the thermal diffusivity and thermal conductivity of the investigated SiAlCN1 and SiAlCN2 samples and those reported values for Si—C—N by Santhosh et al.[44] Both samples display similar and comparable thermal diffusivity values, but exhibit distinguishable trends and values for thermal conductivity. The thermal conductivity of SiAlCN2 increases gradually from 0.6 W m^{-1} K^{-1} at room temperature to 0.8 W m^{-1} K^{-1} at 900°C. The observed thermal conductivity trend is consistent with previously reported behavior in Si—O—C glasses and glass ceramics[48] as well as in Si—C—N ceramics.[44] A more rigid and ordered bonding environment in SiAlCN2, dominated by SiN_4 units may increase phonon scattering due to reduced vibrational freedom and increased network rigidity and result in lower thermal conductivity despite its slightly higher bulk density as compared to that of SiAlCN1.

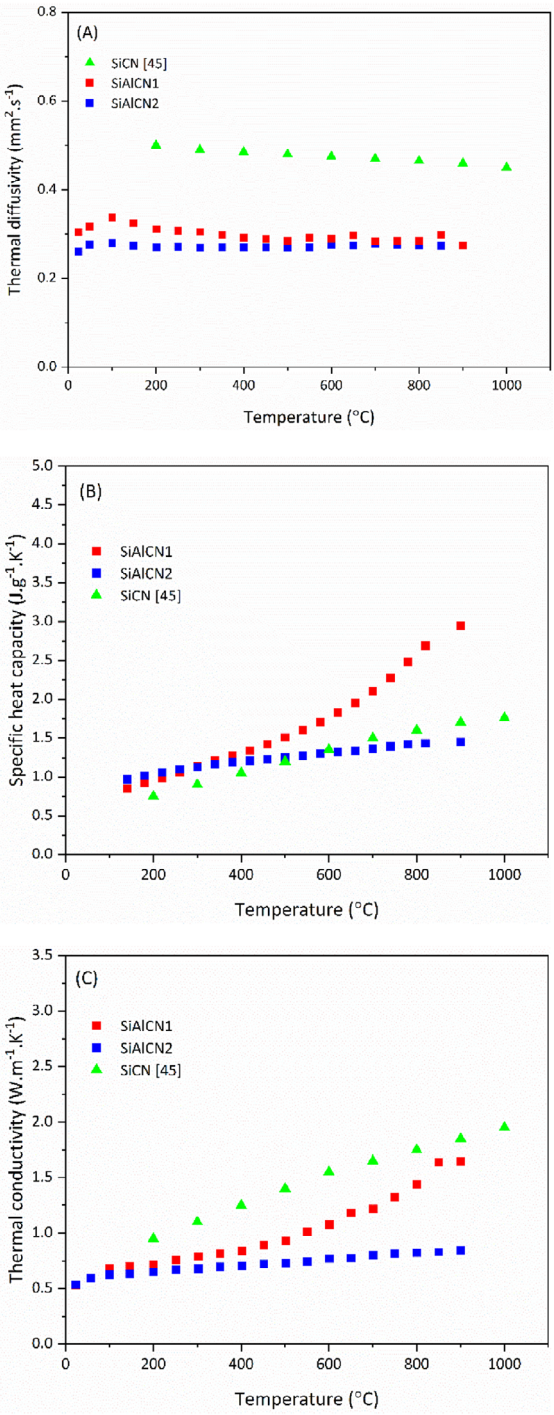

FIGURE 11 Thermal diffusivity (A), specific heat capacity (B), and thermal conductivity (C) of SiAlCN1, SiAlCN2, and SiCN.[44]

3.4 | Nanoindentation study on the Si—Al—C—N-based ceramic monoliths

Nanoindentation tests were performed on monolithic SiCN, SiAlCN1, and SiAlCN2 pyrolyzed at 1000°C (Figure 12).

TABLE 3 Reduced elastic modulus and hardness of SiCN, SiAlCN1, and SiAlCN2 prepared via pyrolysis at 1000°C in argon obtained from nanoindentation experiment.

Sample	Average reduced elastic modulus (GPa)	Average hardness (GPa)
SiCN	163 ± 22	13.6 ± 5.7
SiAlCN1	157 ± 17	15.4 ± 3.2
SiAlCN2	156 ± 18	14.5 ± 4.8

The average measured hardness and modulus values listed in Table 3, which were extracted from the plateau region of the hardness–displacement (Figure 13A) and modulus–displacement (Figure 13B) plots in the range of 500–1500 nm, following the Oliver and Pharr[37] method to minimize surface effects and better reflect intrinsic material hardness.

All samples exhibit hardness values in the range of 14.7–15.3 GPa, while the Young's modulus slightly decreases from 163 GPa in SiCN to 157 GPa in SiAlCN2 with increasing Al content. Despite improved densification found in Al-modified samples, hardness remains nearly unchanged. While many studies have focused on the mechanical behavior of crystalline Si–C–N-based ceramics, the structure–property relationships in amorphous systems remain less explored. Liu et al. highlighted this gap by computational investigations using ab initio molecular dynamics simulations based on density functional theory to study the structural and mechanical properties of amorphous SiBCN ceramics with varying compositions and showing that their mechanical performance is closely tied to local bonding configurations rather than long-range order.[49] In agreement with their findings, our results demonstrate that in the absence of long-range ordering, mechanical properties are governed predominantly by the short-range atomic structure, rather than by bulk density or residual porosity. The load–displacement curves obtained from nanoindentation show a clear contrast between the porous SiCN (Figure 12A) and the denser SiAlCN2 (Figure 12B). Sample SiCN, which contains ~23 vol% porosity, exhibits a less smooth indentation response with visible instabilities. These fluctuations are attributed to pore collapse or local soft zones under the indenter. In contrast, SiAlCN2, which exhibits reduced porosity, shows a smooth and continuous load–displacement curve, indicative of a more homogeneous mechanical response. Similar behavior has been reported by Bernauer et al. for SiC/(Hf,Ta)C(N)/(B)C ceramic composites synthesized via spark plasma sintering,[50] and by Guo et al. for SiC whisker-reinforced Si—Al—C—N ceramics also fabricated by spark plasma sintering.[51,52] Both studies concluded that residual porosity leads to discontinuities

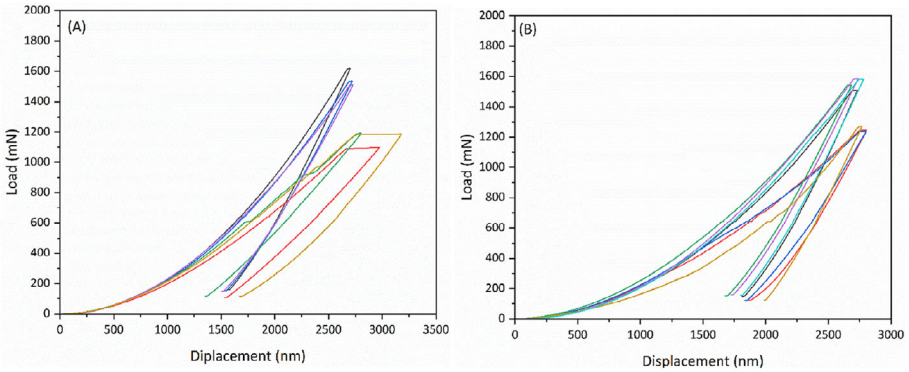

FIGURE 12 Load–displacement curves of SiCN (A) and SiAlCN2 (B) ceramics.

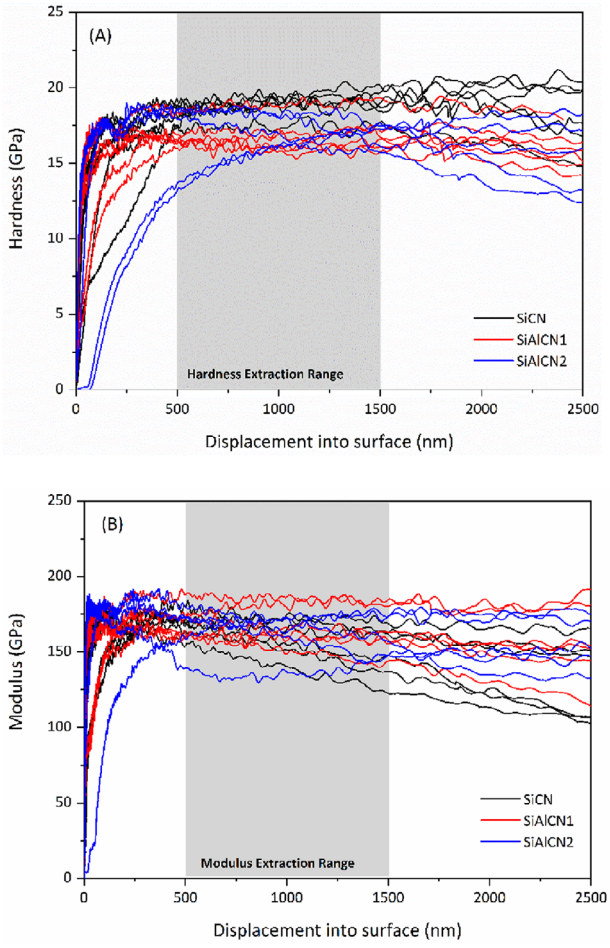

FIGURE 13 Nanoindentation hardness (A) and modulus (B) of SiCN, SiAlCN1, and SiAlCN2 prepared via pyrolysis at 1000°C in argon.

in indentation curves, irrespective of the crystalline nature of the material. Furthermore, Li et al. directly addressed the influence of porosity, noting that elevated porosity levels can induce elastic–plastic instabilities beneath the indenter, resulting in pronounced curve fluctuations.[50] These findings underscore the critical role of porosity in determining mechanical properties via nanoindentation.

4 | CONCLUSION

Polyaluminosilazane was synthesized through the chemical modification of commercially available poly(organo)silazane with tris(dimethylamido)aluminum via a single-source precursor route. Monolithic Si—Al—C—N ceramics were subsequently fabricated using aluminum-modified precursors subsequently consolidated into dense, crack-free monolithic parts with porosity of ~2–4 vol% through a controlled solid–liquid mixing methodology. TGA revealed a high ceramization yield of approximately 90% for the aluminum-rich sample. Powder XRD analysis of the annealed samples revealed that increased aluminum incorporation favors the crystallization of AlN and β-Si_3N_4 upon annealing at high temperatures, while concurrently suppressing β-SiC formation. Solid-state MAS NMR of the bulk samples confirmed the incorporation of aluminum into the amorphous SiCN network and an elevated presence of tetrahedrally coordinated SiN_4 units in the Al-rich compositions, indicating a more crosslinked network architecture as compared to that of the Al-free system. The monolithic SiAlCN2 ceramic with higher amount of Al content exhibited ultra-low thermal conductivity of 0.6 and 0.8 W m^{-1} K^{-1} at room temperature and at 900°C, respectively, making them promising candidates for high-temperature thermal insulation applications. Despite similar thermal diffusivity and bulk density, the sample with higher Al content demonstrated lower thermal conductivity, attributed to its reduced specific heat capacity and more rigid bonding configuration. These findings highlight that compositional tuning of aluminum content within Si—Al—C—N systems is a viable strategy to modulate network structure and thermophysical behavior, advancing the development of high-performance ceramics for the use in extreme thermal environments.

ACKNOWLEDGMENTS

The authors thank the German Science Foundation (Deutsche Forschungsgemeinschaft Bonn) for financial

support within the research training group 2561 "MatCom-ComMat: Materials Compounds from Composite Materials for Applications in Extreme Conditions" (project number: 413956820). Furthermore, the assistance in nanoindentation experiments by Dr. Sebastian Bruns (TU Darmstadt, Institute for Materials Science, Prof. Karsten Durst) and DSC measurements by Dr. Sandipan Sen (KIT, Institute for Applied Materials, Prof. M. Heilmaier) is gratefully acknowledged.

ORCID

Marc Widenmeyer https://orcid.org/0000-0003-4746-7030
Wenjie Xie https://orcid.org/0000-0003-1826-7574
Astrid Pundt https://orcid.org/0000-0002-6665-6745
Gerd Buntkowsky https://orcid.org/0000-0003-1304-9762
Ralf Riedel https://orcid.org/0000-0001-6888-7208
Emanuel Ionescu https://orcid.org/0000-0002-3266-3031

REFERENCES

1. Vagge ST, Ghogare S. Thermal barrier coatings: review. Mater Today: Proc. 2022;56:1201–16. https://doi.org/10.1016/j.matpr.2021.11.170
2. Leach F, Kalghatgi G, Stone R, Miles P. The scope for improving the efficiency and environmental impact of internal combustion engines. Transport Eng. 2020;1:100005. https://doi.org/10.1016/j.treng.2020.100005
3. Levi CG. Emerging materials and processes for thermal barrier systems. Curr Opin Solid State Mater Sci. 2004;8:77–91. https://doi.org/10.1016/j.cossms.2004.03.009
4. Masera K, Hossain AK. Biofuels and thermal barrier: a review on compression ignition engine performance, combustion and exhaust gas emission. J Energy Inst. 2019;92:783–801. https://doi.org/10.1016/j.joei.2018.02.005
5. Tejero-Martin D, Bennett C, Hussain T. A review on environmental barrier coatings: history, current state of the art and future developments. J Eur Ceram Soc. 2021;41:1747–68. https://doi.org/10.1016/j.jeurceramsoc.2020.10.057
6. Aydın S, Sayın C. Impact of thermal barrier coating application on the combustion, performance and emissions of a diesel engine fueled with waste cooking oil biodiesel–diesel blends. Fuel. 2014;136:334–40. https://doi.org/10.1016/j.fuel.2014.07.074
7. Vaßen R, Jarligo MO, Steinke T, Mack DE, Stöver D. Overview on advanced thermal barrier coatings. Surf Coatings Technol. 2010;205:938–42. https://doi.org/10.1016/j.surfcoat.2010.08.151
8. Liu L, Wang S, Zhang B, Jiang G, Liu H, Yang J, et al. Present status and prospects of nanostructured thermal barrier coatings and their performance improvement strategies: a review. J Manuf Process. 2023;97:12–34. https://doi.org/10.1016/j.jmapro.2023.04.052
9. Li X, Zhang W, Cai X. Mechanical evaluation of thermal barrier coatings by indentation: a review. J Mater Res Technol. 2024;30:5402–16. https://doi.org/10.1016/j.jmrt.2024.04.258
10. Jiang J, Xue Y, Li J, Zhang C, Hu X, Yan L, et al. Microwave absorption and thermal insulation integrated polymer-derived SiBCN/SiBCNnf ceramic aerogel with enhanced mechanical property. Ceram Int. 2024;50:41527–33. https://doi.org/10.1016/j.ceramint.2024.08.002
11. Chen L, Li B, Feng J. Rare-earth tantalates for next-generation thermal barrier coatings. Prog Mater Sci. 2024;144:101265. https://doi.org/10.1016/j.pmatsci.2024.101265
12. Clarke DR, Oechsner M, Padture NP. Thermal-barrier coatings for more efficient gas-turbine engines. MRS Bull. 2012;37:891–98. https://doi.org/10.1557/mrs.2012.232
13. Barrios E, Zhai L. A review of the evolution of the nanostructure of SiCN and SiOC polymer derived ceramics and the impact on mechanical properties. Mol Syst Design Eng. 2020;5:1606–41. https://doi.org/10.1039/D0ME00123F
14. Ren Z, Mujib SB, Singh G. High-temperature properties and applications of Si-based polymer-derived ceramics. Materials. 2021;14:614. https://doi.org/10.3390/ma14030614
15. Feng B, Peter J, Fasel C, Wen Q, Zhang Y, Kleebe H-J, et al. High-temperature phase and microstructure evolution of polymer-derived SiZrCN and SiZrBCN ceramic nanocomposites. J Am Ceram Soc. 2020;103:7001–13. https://doi.org/10.1111/jace.17149
16. Colombo P, Mera G, Riedel R, Sorarù GD. Polymer-derived ceramics: 40 years of research and innovation in advanced ceramics. J Am Ceram Soc. 2010;93:1805–37. https://doi.org/10.1111/j.1551-2916.2010.03876.x
17. Leonel GJ, Guo X, Singh G, Navrotsky A. Chemistry, structure, and thermodynamic stabilization of SiOC polymer derived ceramics made from commercial precursors. Open Ceram. 2023;15:1–9.
18. Torrey JD, Bordia RK. Phase and microstructural evolution in polymer-derived composite systems and coatings. J Mater Res. 2007;22:1959–66. https://doi.org/10.1557/jmr.2007.0246
19. Wang Y, Ding J, Feng W, An L. Effect of pyrolysis temperature on the piezoresistivity of polymer-derived ceramics. J Am Ceram Soc. 2011;94:359–62. https://doi.org/10.1111/j.1551-2916.2010.04330.x
20. Zhao R, Shao G, Cao Y, An L, Xu C. Temperature sensor made of polymer-derived ceramics for high-temperature applications. Sens Actuators A: Phys. 2014;219:58–64. https://doi.org/10.1016/j.sna.2014.08.012
21. Papendorf B, Nonnenmacher K, Ionescu E, Kleebe HJ, Riedel R. Strong influence of polymer architecture on the microstructural evolution of hafnium-alkoxide-modified silazanes upon ceramization. Small. 2011;7:970–78. https://doi.org/10.1002/smll.201001938
22. Ionescu E, Kleebe HJ, Riedel R. Silicon-containing polymer-derived ceramic nanocomposites (PDC-NCs): preparative approaches and properties. Chem Soc Rev. 2012;41:5032. https://doi.org/10.1039/c2cs15319j
23. Wang ZC, Aldinger F, Riedel R. Novel silicon-boron-carbon-nitrogen materials thermally stable up to 2200°C. J Am Ceram Soc. 2001;84:2179–83. https://doi.org/10.1111/j.1151-2916.2001.tb00984.x
24. An L, Riedel R, Konetschny C, Kleebe H-J, Raj R. Newtonian viscosity of amorphous silicon carbonitride at high temperature. J Am Ceram Soc. 1998;81:1349–52. https://doi.org/10.1111/j.1151-2916.1998.tb02489.x

25. Yu Y, Li J, Niu J, Yi F, Meng S. Preparation and temperature-resistance characteristics of novel dense SiAlCN ceramics. Ceram Int. 2018;44:22473–80. https://doi.org/10.1016/j.ceramint.2018.09.016
26. Liew LA, Bright VM, Raj R. A novel micro glow plug fabricated from polymer-derived ceramics: in situ measurement of high-temperature properties and application to ultrahigh-temperature ignition. Sens Actuators A: Phys. 2003;104:246–62. https://doi.org/10.1016/S0924-4247(03)00027-X
27. Jacobson NS. Corrosion of Silicon-based ceramics in combustion environments. J Am Ceram Soc. 1993;76:3–28. https://doi.org/10.1111/j.1151-2916.1993.tb03684.x
28. Jacobson NS, Fox DS, Opila EJ. High temperature oxidation of ceramic matrix composites. Pure Appl Chem. 1998;70:493–500. https://doi.org/10.1351/pac199870020493
29. An L, Wang Y, Bharadwaj L, Zhang L, Fan Y, Jiang D, et al. Silicoaluminum carbonitride with anomalously high resistance to oxidation and hot corrosion. Adv Eng Mater. 2004;6:337–40. https://doi.org/10.1002/adem.200400010
30. Wang Y, Fan Y, Zhang L, Zhang W, An L. Polymer-derived SiAlCN ceramics resist oxidation at 1400°C. Scr Mater. 2006;55:295–97. https://doi.org/10.1016/j.scriptamat.2006.05.004
31. Dhamne A, Xu W, Fookes BG, Fan Y, Zhang L, Burton S, et al. Polymer–ceramic conversion of liquid polyaluminasilazanes for SiAlCN ceramics. J Am Ceram Soc. 2005;88:2415–19. https://doi.org/10.1111/j.1551-2916.2005.00481.x
32. Wang Y, Fei W, An L. Oxidation/corrosion of polymer-derived SiAlCN ceramics in water vapor. J Am Ceram Soc. 2006;89:1079–82. https://doi.org/10.1111/j.1551-2916.2005.00791.x
33. Wang Y, An L, Fan Y, Zhang L, Burton S, Gan Z. Oxidation of polymer-derived SiAlCN ceramics. J Am Ceram Soc. 2005;88:3075–80. https://doi.org/10.1111/j.1551-2916.2005.00542.x
34. Jiang T, Hill A, Fei W, Wei Y, Tellam M, Xu C, et al. Making bulk ceramics from polymeric precursors. J Am Ceram Soc. 2010;93:3017–19. https://doi.org/10.1111/j.1551-2916.2010.04069.x
35. Sun ZL, Zhou Y, Jia DC, Duan XM, Yang ZH, Ye D, et al. Mechanical and thermal physical properties of amorphous SiCN(O) ceramic bulks prepared by hot-press sintering. Mater Lett. 2012;72:57–59. https://doi.org/10.1016/j.matlet.2011.12.053
36. Riedel R, Passing G, Schönfelder H, Brook RJ. Synthesis of dense silicon-based ceramics at low temperatures. Nature. 1992;355:714–17. https://doi.org/10.1038/355714a0
37. Oliver WC, Pharr GM. Measurement of hardness and elastic modulus by instrumented indentation: advances in understanding and refinements to methodology. J Mater Res. 2004;19:3–20. https://doi.org/10.1557/jmr.2004.19.1.3
38. Bernauer J. Advanced engineering materials polymer-derived ceramic coatings with excellent thermal cycling stability. PhD Thesis. TU Darmstadt. 2025.
39. Wang J, Schölch V, Görke O, Schuck G, Wang X, Shao G, et al. Metal-containing ceramic nanocomposites synthesized from metal acetates and polysilazane. Open Ceram. 2020;1:100001.
40. Ionescu E, Papendorf B, Kleebe H-J, Breitzke H, Nonnenmacher K, Buntkowsky G, et al. Phase separation of a hafnium alkoxide-modified polysilazane upon polymer-to-ceramic transformation—a case study. J Eur Ceram Soc. 2012;32:1873–81. https://doi.org/10.1016/j.jeurceramsoc.2011.09.003
41. Yuan J, Hapis S, Breitzke H, Xu Y, Fasel C, Kleebe H-J, et al. Single-source-precursor synthesis of hafnium-containing ultrahigh-temperature ceramic nanocomposites (UHTC-NCs). Inorg Chem. 2014;53(19):10443–55. https://doi.org/10.1021/ic501512p
42. Berger F, Weinmann M, Aldinger F, Müller K. Solid-State NMR studies of the preparation of Si—Al—C—N ceramics from aluminum-modified polysilazanes and polysilylcarbodiimides. Chem Mater. 2004;16:919–29. https://doi.org/10.1021/cm0351700
43. Salameh C, Bernard S, Gervais C, Babonneau F, Bruma A, Malo S, et al. Chemistry of a series of aluminum-modified polysilazanes: synthesis, pyrolysis behaviour and microstructural evolution. J Eur Ceram Soc. 2019;39:183–94. https://doi.org/10.1016/j.jeurceramsoc.2018.09.027
44. Santhosh B, Biesuz M, Sorarù GD. Thermal properties of dense polymer-derived SiCN(O) glasses. Mater Lett. 2021;288:129336. https://doi.org/10.1016/j.matlet.2021.129336
45. Song J, Mo G, Wu X, He L, Huang Q, Huang Z. Facile synthesis of a carbon-rich SiAlCN precursor and investigation of its structural evolution during the polymer–ceramic conversion process. Ceram Int. 2022;48:3311–27. https://doi.org/10.1016/j.ceramint.2021.10.107
46. Sen S, Widgeon S. On the mass fractal character of Si-based structural networks in amorphous polymer derived ceramics. Nanomaterials. 2014;5:366–75. https://doi.org/10.3390/nano5010366
47. Touloukian YS, Buyco EH. Thermophysical properties of matter—the TPRC data series. Specific heat—nonmetallic solids. Vol. 5. 1970. p. 1730.
48. Stabler C, Reitz A, Stein P, Albert B, Riedel R, Ionescu E. Thermal properties of SiOC glasses and glass ceramics at elevated temperatures. Materials. 2018;11:279. https://doi.org/10.3390/ma11020279
49. Liu Y, Zhou Y, Jia D, Yang Z, Duan W, Li D, et al. Composition-dependent structural characteristics and mechanical properties of amorphous SiBCN ceramics by ab-initio calculations. J Adv Ceram. 2023;12:984–1000. https://doi.org/10.26599/JAC.2023.9220733
50. Bernauer J, Petry NC, Thor N, Kredel SA, Teppala DT, Galetz M, et al. Exceptional hardness and thermal properties of SiC/(Hf,Ta)C(N)/(B)C ceramic composites derived from single-source precursor. Adv Eng Mater. 2024;26(17):2301864. https://doi.org/10.1002/adem.202301864
51. Guo R, Li Z, Li L, Zheng R, Ma C. Toughening mechanism and oxidation resistance of SiC whisker-toughened SiAlCN ceramics. Ceram Int. 2024;50:8853–64. https://doi.org/10.1016/j.ceramint.2023.12.201
52. Li Z, Guo R, Li L, Zheng R, Ma C. Microstructure and fracture toughness of SiAlCN ceramics toughened by SiCw or GNPs. Ceram Int. 2023;49:29709–18. https://doi.org/10.1016/j.ceramint.2023.06.211

How to cite this article: Boroojerdi M, Camacho D, Breitzke H, Nurak I, Widenmeyer M, Xie W. et al., Synthesis and thermal properties of dense Si—Al—C—N-based polymer-derived ceramics. Int J Appl Ceram Technol. 2025;e70119. https://doi.org/10.1111/ijac.70119